Study of the swirling flow field induced by guide vanes using electrical resistance tomography and numerical simulations

Jing-zun Zhang, Hua Li, Jian-wen Ma, Xiao-ping Chen & Jing-yu Xu

Taylor & Francis
Taylor & Francis Group

Check for updates

Study of the swirling flow field induced by guide vanes using electrical resistance tomography and numerical simulations

Jing-zun Zhang[a,b,c], Shuo Liu[b,d], Hua Li[b,d], Xiao-ping Chen[b,d], Jian-wen Ma[a], and Jing-yu Xu[b,d]

[a]Institute of Remote Sensing and Digital Earth, Chinese Academy of Sciences, Beijing, China; [b]University of Chinese Academy of Sciences, Beijing, China; [c]College of Intellectualized City, Beijing Union University, Beijing, China; [d]Institute of Mechanics, Chinese Academy of Sciences, Beijing, China

ABSTRACT

In this work, the swirling flow field induced by guide vanes was studied using electrical resistance tomography (ERT) and numerical simulations. The results show that the two-phase water and oil mixture moves in the same axial direction for this type of flow field, which is very unlike the flow behavior of a traditional hydrocyclone with a tangential inlet. In the pipe behind the guide vanes, the smallest axial velocity and tangential velocity are located at the center of the pipe. From the pipe center to the pipe wall, both pressure and velocity increase gradually. Downstream of guide vanes, the maximal oil volume fraction is observed at the center of the pipe. From the center of the pipe to the inner wall, the oil volume fraction gradually decreases. Moreover, ERT can precisely show the oil distribution in the pipe section. These studies prove the possibility of efficient oil and water mixture separation by guide vanes, and the results may be very important for guiding the optimal design of vane-type pipe separators.

Introduction

The separation of oil–water two-phase dispersion is important in the process of oil production, and the use of hydrocyclones is not uncommon in the petroleum industry. To date, much progress has been made in the research on swirling flow fields inside a hydrocyclone (Zhou et al., 2010). However, due to the different structural parameters of each hydrocyclone, there are great differences in the swirling flow fields. Gao et al. (2011) studied the flow velocity of hydrocyclones with a tangential inlet. The results showed that several asymmetric envelopes of equal vertical velocities existed during the upward inner flows and downward outer flows. While the increase in the feed pressure has little influence on the distribution characteristics of the vertical and tangential velocities, the magnitude and gradient of the tangential velocity were noticeably enlarged in the hydrocyclones. Marins et al. (2010) researched the flow field in the hydrocyclones experimentally without the air core using Laser Doppler Anemometry (LDA) and particle image velocimetry (PIV). The exponent n in the tangential

velocity equation was determined to be approximately 0.61. The turbulence in the axial direction was observed to be slightly higher than that in the tangential direction. For an axial flow hydrocyclone, Wang et al. (2011) studied the internal flow field using computational fluid dynamics (CFD) techniques and Laser Doppler Velocimetry (LDV) tests. It was found that the guide vanes may divide the fluid evenly and effectively prevent the eccentricity. Furthermore, the pressure in hydrocyclone was also studied, and the specific effects of the guide vanes were described.

More recently, Ahmed et al. (2015) experimentally investigated the effects of swirl on the impingement surface pressure for an incompressible, turbulent, swirling impinging air jet. The effect of swirl number, nozzle-to-plate distance, and Reynolds number on the pressure distribution was examined. The results showed that for medium-to-high swirls, the maximum pressure coefficient shifted radically outward from the stagnation point and became relatively flat with increasing swirl number. The stagnation pressure decreased nonlinearly with increasing swirl

---

intensity and followed a quadratic relationship for a given Reynolds number. Wannassi and Monnoyer (2016) studied the dynamics behavior of the flow generated by blade swirlers. The results obtained for different configurations revealed that a vertical structure was present at the inlet of the swirl generator and was identified at the jet exit. Its intensity depended on the blade angle. Javadi et al. (2016) investigated the flow unsteadiness generated in a swirl apparatus experimentally and numerically. The experimental results showed that the largest on-axis recirculation region, the largest precessing vortex rope, and the highest level of velocity fluctuations occurred at the lowest rotational speed, and the processing vortex rope counter-rotated the runner.

The new vane-type pipe separator uses the guide vanes to produce swirling flow fields to realize centrifugal oil–water separation (Shi et al., 2012; Shi and Xu, 2015). However, the flow characteristics of the swirling flow field are not very clear because of the unique structure of the guide vanes. In this work, the phase distribution in the pipe cross section was obtained using electrical resistance tomography (ERT). Combined with the results of numerical simulations, the flow characteristics and the oil distribution at different axial distances are presented. These results may be of great significance for guiding the optimal design of vane-type pipe separators. To achieve this goal, numerical simulations and experiments were performed. The experimental method and equipment are presented in "experimental study." Then, the geometric model and numerical setup of the simulation are described in "numerical simulation." The results and analysis section mainly focuses on the pressure drop, velocity distribution, and the oil volume fraction distribution.

Experimental study

Measurement method

The key parameters in the experiment were the pressure drop and section phase volume fraction. The pressure drop can be measured by a pressure sensor, together with the DAQP-12H data acquisition system with the sampling frequency of 2000 Hz. For section phase volume fraction measurements, ERT was an ideal choice. ERT is a kind of noninvasive industrial process tomography that can retrieve internal information from the pipe without interfering with the flow field (Wang et al., 2003; Li et al., 2005; Olerni et al., 2013). The ERT instrument used in this experiment is an ITS Z8000 system, which can obtain the phase distribution by measuring the voltages of the electrodes. In each plane, 16 stainless steel electrodes are mounted flush to the surface at equal intervals without disturbing the inner fluids. Using the conductivity data obtained by ERT, the local volume fraction distribution (α) can be determined using Maxwell's equation (Maxwell, 1881):

$$\alpha = \frac{2\sigma_1 + \sigma_2 - 2\sigma_{\mathrm{mc}} - \sigma_{\mathrm{mc}}\frac{\sigma_2}{\sigma_1}}{\sigma_{\mathrm{mc}} - \sigma_{\mathrm{mc}}\frac{\sigma_2}{\sigma_1} + 2(\sigma_1 - \sigma_2)} \qquad (1)$$

where σ_1 is the conductivity of the first phase, σ_2 is the conductivity of the second phase, and σ_{mc} is the local mix conductivity distribution. A more detailed description of the operational principle of ERT can be found in the works of Wu et al. (2005).

In this work, there were two circles of electrodes, named section I and section II, which were placed 12R and 42R downstream of the guide vanes, relative to the developing period and the stable period of the swirling flow field, respectively. The concentration profile obtained using ERT could have a certain error due to the high sensitivity of various factors such as the accuracy of the electrical measurement made at the system boundary and the image reconstruction algorithm used. A reference measurement error of 1% could lead to a conductivity error of up to 10% depending on the magnitude of the conductivity charge (Wang et al., 1999). In this work, before collecting data, we calibrated the ERT system and took the reference frame when the sensor was full of liquid only so that the reference measurement error could be controlled within 0.5%. Thus, the relative errors of the cross-sectional average oil volume fraction were found to be smaller than 5%. Moreover, pressure sensors were installed at locations 40R and 24R upstream.

Materials and vane configuration

In this work, tap water and industrial white oil PS-40, produced by the Yanshan Petrochemical Company in China, were used to prepare the oil–water dispersions. The white oil was a refined mineral oil consisting of saturated hydrocarbons and can be classified based on the viscosity. At 20°C, the density of white oil was 840 kg/m^3 with
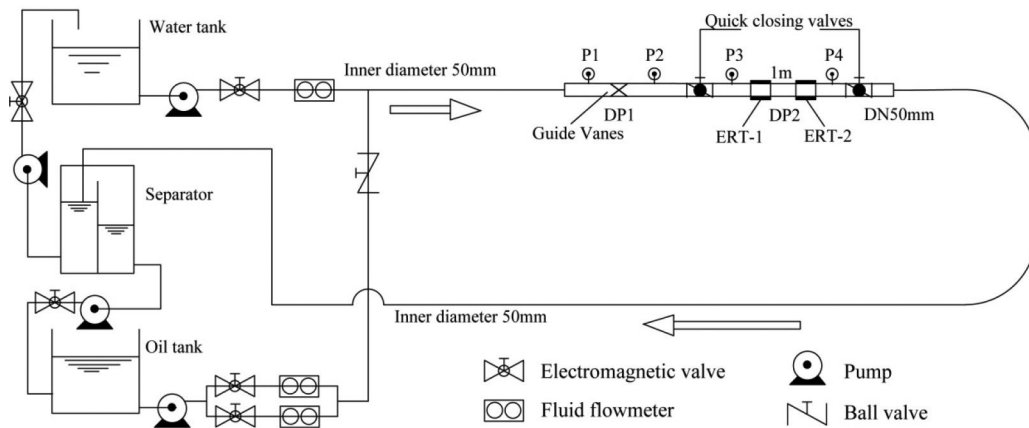
Figure 1. Schematic view of the flow loop.

the viscosity of 36 mPa · s. The density of tap water was 998 kg/m³ with the viscosity 1.0 mPa. All experiments were conducted at approximately 20°C.

Since this work is mainly concerned with the oil phase concentration in the swirling flow field, equipment creating a swirling flow field was essential. The guide vane was applied as the swirling instrument. The guide vanes were two pieces of thin, semicircular plates, and the deflector angle of the guide vanes to the pipe section was 45°, as shown in Figures 1 and 2.

Experimental design and operating methods

The experiments were performed on the multiphase flow experimental platform in the Institute of Mechanics, Chinese Academy of Sciences. A schematic view of the flow loop is depicted in Figure 1. The flow loop consisted of transparent Perspex pipes with the inner diameter of 50 mm, which was helpful for better observing the flow field. Guide vanes were placed in the pipe with the pressure sensors upstream and downstream for the pressure drop measurement. Two ERT electrodes were placed downstream of the guide vanes with reasonable distance for the oil core development. In the experiment, both oil and water were first measured by a turbine flow meter and an electromagnetic flow meter, respectively, and were then mixed by a T-junction. Finally, oil and water flowed into the separating tank for gravity separation.

Data matrix

During the experiment, the water flow rate at the entrance was fixed at first, and the inlet oil volume fraction (β) was adjusted from 0 to 0.2 gradually, while the water flow rates changed from 3.0 to 12.0 m³/s with 3 m³/h intervals. For each operating condition, the pressure data and the section oil distribution information were recorded for future analysis.

Numerical simulation

Numerical simulation model

The numerical simulation was conducted with the Fluent commercial software, which uses the finite volume method to discretize the differential equations describing the multiphase flow, and the Reynolds stress model (RSM) model was chosen to perform the simulation with the mixture multiphase flow model applied to simulate the oil–water flow. The mathematical model for the mixture multiphase flow is as follows:

$$\frac{\partial}{\partial t}(\rho_m) + \nabla \cdot (\rho_m \vec{v}_m) = \dot{m} \qquad (2)$$
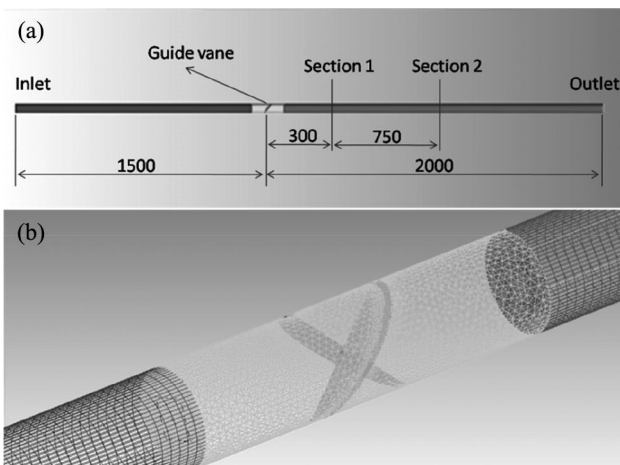

Figure 2. View of the computational domain.

where $\vec{v}_m$ is the average velocity, ρ_m is the mixture density, and $\dot{m}$ is the user-defined mass transfer of the mass source. The variables $\vec{v}_m$ and ρ_m can be obtained according to the following equations:

$$\vec{v}_m = \frac{\sum_{k=1}^{n} \alpha_k \rho_k \vec{v}_k}{\rho_m} \tag{3}$$

$$\rho_m = \sum_{k=1}^{n} \alpha_k \rho_k \tag{4}$$

$$\frac{\partial}{\partial t}(\rho_m \vec{v}_m) + \nabla \cdot (\rho_m \vec{v}_m \vec{v}_m)$$
$$= -\nabla P + \nabla \cdot \left[\mu_m\left(\nabla \vec{v}_m + \nabla \vec{v}_m^T\right)\right] + \rho_m \vec{g} + \vec{F}$$
$$+ \nabla \cdot \left(\sum_{k=1}^{n} \alpha_k \rho_k \vec{v}_{dr,k} \vec{v}_{dr,k}\right) \tag{5}$$

where n is the number of the phases, $\vec{F}$ is the body force, μ_m is the mixture viscosity, and $\vec{v}_{dr,k}$ is the drift velocity of the kth phase. The variables $\vec{v}_{dr,k}$ and μ_m can be obtained according to the following equations:

$$\mu_m = \sum_{k=1}^{n} \alpha_k \mu_k \tag{6}$$

$$\vec{v}_{dr,k} = \vec{v}_k - \vec{v}_m \tag{7}$$

As for the turbulent model, the equation of the RSM model is as follows:

$$\frac{\partial}{\partial t}(\rho \overline{u_i u_j}) + \frac{\partial}{\partial x_k}(\rho U_k \overline{u_i u_j})$$

$$= -\underbrace{\frac{\partial}{\partial x_k}\left[\rho \overline{u_i u_j u_k} + \overline{p u_j}\delta_{ik} + \overline{p u_i}\delta_{jk}\right]}_{D_{T,ij} \equiv \text{Turbulent Diffusion}}$$

$$+ \underbrace{\frac{\partial}{\partial x_k}\left(\mu \frac{\partial}{\partial x_k}\overline{u_i u_j}\right)}_{D_{L,ij} \equiv \text{Molecular Diffusion}} - \underbrace{\rho\left(\overline{u_i u_k}\frac{\partial U_j}{\partial x_k} + \overline{u_j u_k}\frac{\partial U_i}{\partial x_k}\right)}_{P_{ij} \equiv \text{Stress Production}}$$

$$- \underbrace{\rho\beta\left(g_i \overline{u_j \theta} + g_j \overline{u_i \theta}\right)}_{G_{ij} \equiv \text{Buoyancy Production}} + \underbrace{\overline{p\left(\frac{\partial u_i}{\partial x_j} + \frac{\partial u_j}{\partial x_i}\right)}}_{\phi_{ij} \equiv \text{Pressure Strain}}$$

$$- \underbrace{2\mu \overline{\frac{\partial u_i}{\partial x_k}\frac{\partial u_j}{\partial x_k}}}_{\varepsilon_{ij} \equiv \text{Dissipation}} - \underbrace{2\rho\Omega_k\left(\overline{u_j u_m}\varepsilon_{ikm} + \overline{u_i u_m}\varepsilon_{jkm}\right)}_{F_{ij} \equiv \text{Production by System Rotation}}$$

$$+ \underbrace{S_{user}}_{\text{User} - \text{Defined Source Term}} \tag{8}$$

where $D_{T,ij}$ is the turbulent diffusion, $D_{L,ij}$ is the molecular diffusion, P_{ij} is the stress production, G_{ij} is the buoyancy production, φ_{ij} is the pressure strain, ε_{ij} is the dissipation, F_{ij} is the production by system rotation, and the S_{user} is the user-defined term. In the term of buoyancy force, $\beta = -\frac{1}{\rho}\left(\frac{\partial \rho}{\partial T}\right)_P$.

Geometry model character

As with model for numerical simulation, Figure 2a shows the view of the computational domain. The inner diameter of the pipe model was 0.05 m and the pipe model was 3.5 m long in the Y-axis direction. The upstream and downstream extensions of the computational domain with respect to the guide vane position were 1.5 and 2 m, respectively. As seen from Figure 2a, sections I and II were 12R and 42R downstream of the guide vanes, respectively, same as the experimental setup.

The specific structure of guide vanes could be seen clearly in Figure 2b. The guide vanes were two pieces of thin, semicircular plates, and the deflector angle of the guide vanes to the pipe section was 45°. The whole flow field was divided into three parts for meshing according to the structure of the flow field with the assistance of ICEM (Integrated Computer Engineering and Manufacturing). Near the guide vanes (with the length of 200 mm), the computational meshes were generated using unstructured grids due to its geometric properties. Other parts of the geometry model were structural mesh. The sizes of the structural and unstructural grids are coupled to each other. For the structure, all the structural parameters used in the simulation were the same as those used in the above experiment.

Boundary and operating conditions

The boundary conditions were set as follows: the velocity inlet was set to the measured flow velocity magnitude and normal to the inlet surface. The turbulent intensity was set as 5% and the hydraulic diameter was set as the pipe diameter. Since oil and water are both incompressible fluids, the outlet boundary condition was set as outflow. Since this study concentrated on the phase distribution near the pipe center, the wall is defined as a stationary wall with a no slip shearing condition. In addition, the gravitational acceleration was set as −9.8 m/s² in the Z-axis direction.

The operating position was set 24R downstream of the guide vanes at the location of the pressure sensor.

Since the pressure was not uniform in the cross section, the operating position was set near the wall. The operating pressure was set to be the same as the measured value. In this way, the calculated static pressure $40R$ upstream of the guide vanes was exactly the pressure drop measured by the two pressure sensors.

Grid independence study

Figure 3 presents the comparison of the face average velocity magnitude and static pressure change along the fluid domain for different grid qualities. In the figure, coarse, medium, and fine grids were defined as the 168, 642-, 1,164,279-, and 1,912,311-point grids, respectively. The calculation was performed by setting the water flow rate to 9 m³/h and the inlet oil volume fraction to $\beta = 0.107$. From the figure above, it can be seen that the overall trends for the velocity magnitude and static pressure are nearly the same for all grid qualities. However, discrepancies between the medium and fine grids were much smaller than the discrepancies between the coarse grid and the medium grid. As a result, the grid with the medium quality was appropriate for use in numerical simulation in consideration of the calculation accuracy. To reduce the computational cost while preserving the accuracy, the mesh with 1,164,279 grid points was selected for the subsequent calculation.

Solution method

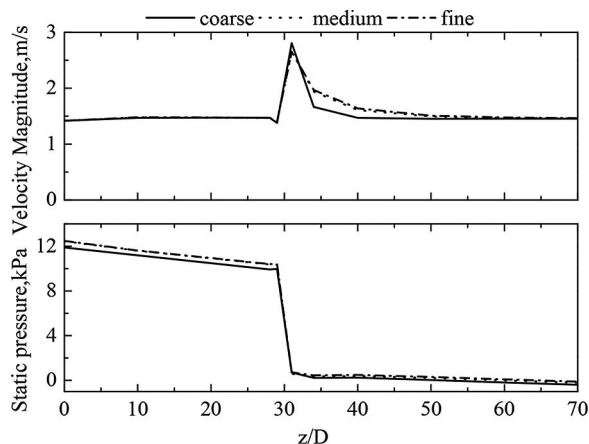Numerical simulation was performed in a steady-state manner considering the flow loop properties.

Figure 3. Comparison of velocity magnitudes and static pressure for different grids.

Considering both the solution convergence and accuracy, the semi-implicit method for pressure-linked equations is applied for the coupling between the pressure and velocity. Discrete formats for the momentum, kinetic energy, turbulent energy dissipation, and Reynolds stress equation are used in a second-order upwind form. The residuals were set to 10^{-5}.

Results and discussion

Comparison of experimental observations and numerical simulations

To confirm that the numerical simulation is reliable, it is essential to compare the results of the numerical simulation to the experimental measurements. On the basis of data matrix discussed in "data matrix," the pressure drop and section phase distribution are chosen as comparison parameters.

For the pressure drop, Figure 4 presents a comparison of the simulated pressure drop and the measured pressure drop. The inlet oil volume fraction is $\beta = 0.107$ and the water flow rate is $Q_w = 3$, 6, 9, and 12 m³/h. Here, the simulated pressure drop is the static pressure near the wall $40R$ upstream of the guide vanes. It is found that the simulated and measured pressure drop values match very well. Moreover, the changing rules of the calculated and measured pressure drops with the inlet water flow rate are also consistent.

For the phase concentrations, Figure 5 shows a comparison of the simulated oil volume fraction (α) in the vertical direction to that measured by ERT. Here, the solid points are the experimental data, and the hollow points are the simulation results. It can be seen that the simulated oil distribution curve matches the experimental curve to some extent. Both the simulated and measured oil fraction decrease as the inlet water flow rate increases. Nevertheless, some deviations are still observed, such as the simulated oil distribution curve being narrower than the experimental curve, which may be because the CFD simulation cannot take the emulsification of the oil–water mixture into account. This has little influence on the overall results. Thus, numerical simulations are reliable for the investigation of the oil–water two-phase swirling flows.
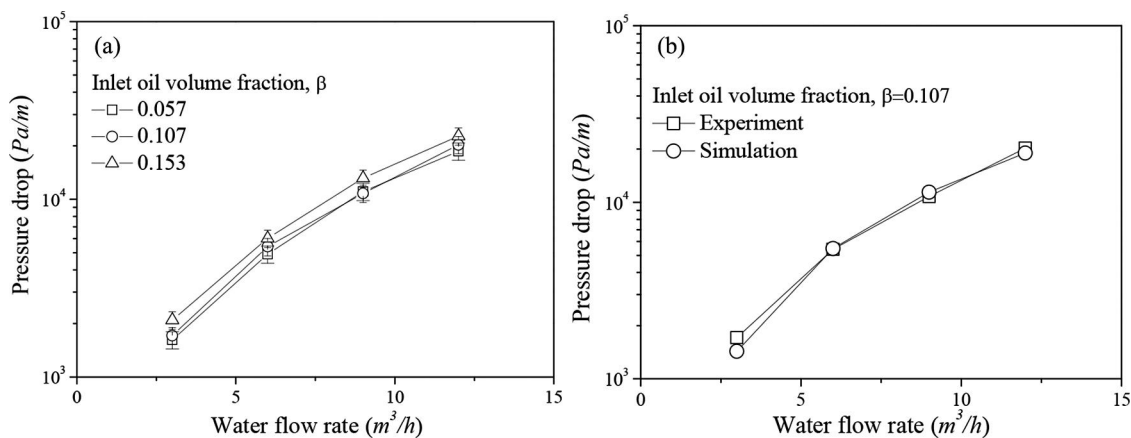
Figure 4. Pressure drop through the guide vanes.

Pressure drop

The pressure drop through the guide vanes is an important indicator of the performance of the vane-type pipe separator. This is because that the larger pressure drop implies a greater energy loss for the separator. The pressure drop through the guide vanes can be divided into two contributions: the local pressure drop caused by the guide vanes and the friction pressure drop in the horizontal pipe upstream and downstream of the guide vanes. Figure 4a shows the pressure drop obtained by subtracting the downstream pressure from the upstream pressure measured by the pressure sensors. When the inlet oil volume fraction is constant, the pressure drop gradually increases with increasing flow rate of the inlet water. However, when the
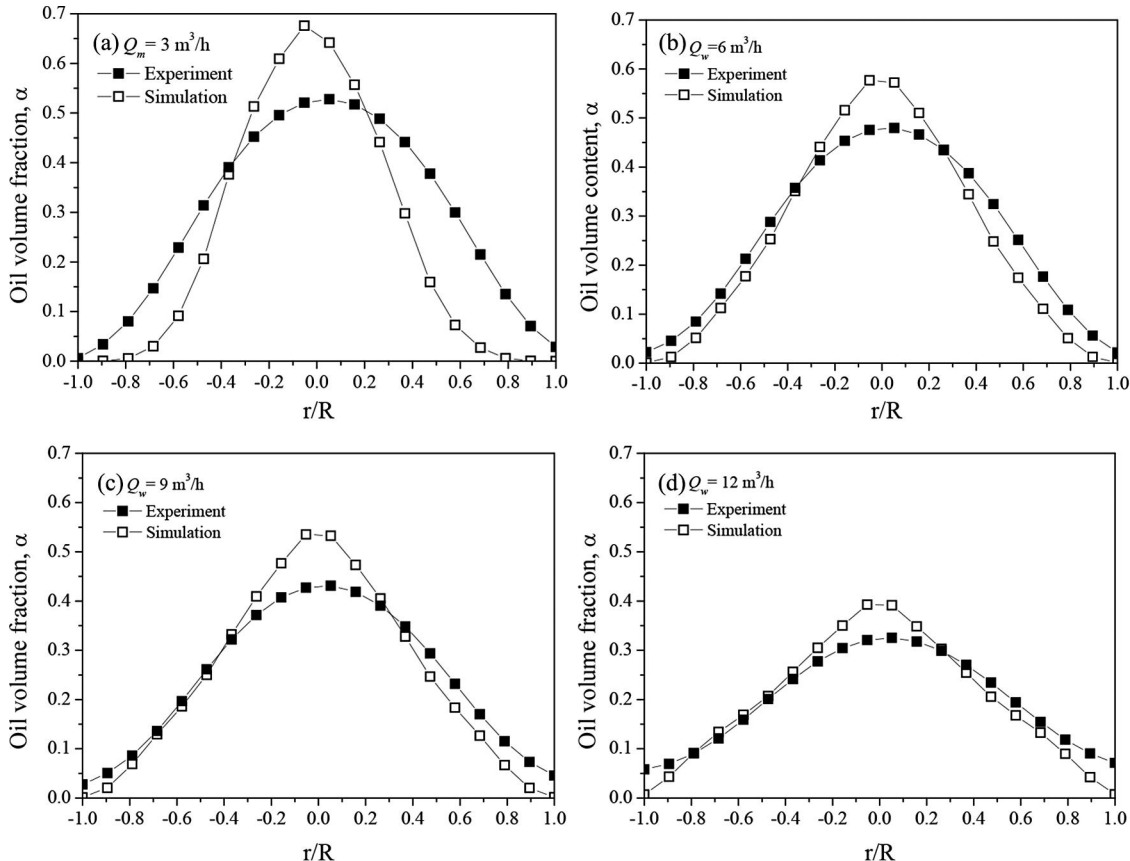

Figure 5. Comparison of oil volume distributions in section I measured with those simulated ($\beta = 0.107$).

water flow rate is constant, higher inlet oil volume fractions correspond to larger pressure drops.

The pressure distribution ($Q_w = 12$ m³/h, $\beta = 0.107$) at section I is shown in Figure 6. In the contour, the dark color means high pressure, while the light color means low pressure with gray as the intermediate value. A low-pressure area occurs at the pipe center. From the pipe center to the pipe wall, the pressure increases gradually. Here, the difference between the maximum pressure and minimum pressure is approximately 2.2 kPa. Taking all the inlet flow rates together, Figure 7 provides a thorough description of the longitudinal pressure distribution for all inlet flow rates with 10.7% oil inlet volume fraction. The red color represents high pressure, while the blue color represents low pressure. For the convenience of analysis, a color map for the pressure contours varies according to the flow rate, as well as that of the streamline. We would like to clarify that as the pressure of the existing domain is set as 0, the pressure in the flow domains is relative pressure. For an individual pressure contour, it can be seen that pressure upstream of the guide vane is higher than that downstream. Furthermore, rotational flow gives rise to the pressure drop at the pipe center. As is shown, the pressure at the pipe center is lower than the pressure near the pipe wall not far away from the vane zone due to the centrifugal force. The lowest pressure appears at the intersection of two vanes, and the low-pressure core gradually dissipates as the rotation intense
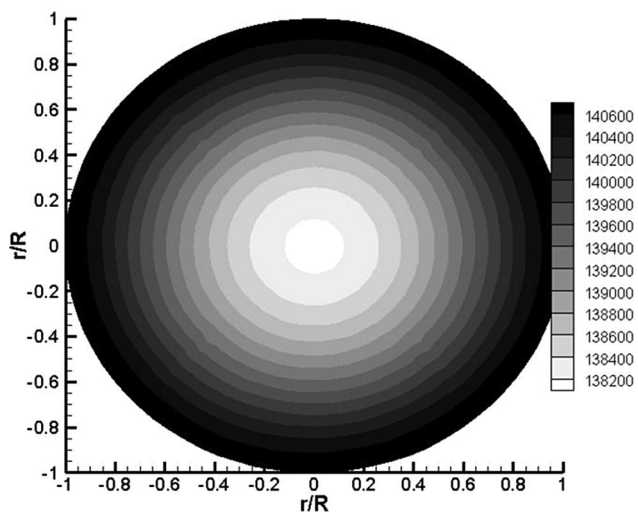
decreases along the tube, for which the trend corresponds to the swirling number change presented in the following study. When the pressure contours of the different inlet flow rate are compared, it is obvious that a higher inlet flow rate results in a steeper pressure drop axially both in the whole fluid domain and the local pressure gradient. In terms of the global pressure drop, it can be seen that global pressure drop varies from 2 to 29 kPa as the inlet flow rate increases from 3 to 12 m³/h. This is due to the configuration of the guide vane itself, which can give rise to an intense hindrance effect when the inlet flow rate is high. For local pressure gradient radially, a higher inlet flow rate produces higher tangential velocity which further steepens pressure gradient radially and results in a higher pressure drop.

Velocity distribution

The velocity distribution was studied based on a CFD simulation performed in the present study. Figure 8 shows the velocity distribution in the longitudinal section colored according to the axial velocity. Here, the inlet water flow rate is $Q_w = 9$ m³/h, and the inlet oil volume fraction is $\beta = 0.107$. The flow field shown in Figure 8 covers the area from $5R$ upstream of the guide vanes to $20R$ downstream of the guide vanes. Upstream of the guide vanes, the axial velocity at the pipe center is slightly larger than that near the pipe wall, and a small radial velocity is present. This is mainly because the influence of buoyancy becomes weak due to the absence of swirl flow. In the area near the guide vanes, an obvious radial component of the velocity was observed. Thus, a highly significant change occurred in the flow direction of the oil–water mixture due to the guide vanes. This change gave rise to the formation of swirling flow field downstream. Downstream of the guide vanes, a large difference in the axial velocity was found. In the radial direction, the axial velocity is much different, and the smallest axial velocity is located at the pipe center just behind the guide vanes. From the center to the wall, the axial velocity increases gradually. In the axial direction, some differences were also found.

Figure 9 provides a thorough depiction of the axial velocity coefficient distribution vertically covering sections from $4R$ to $42R$ downstream.
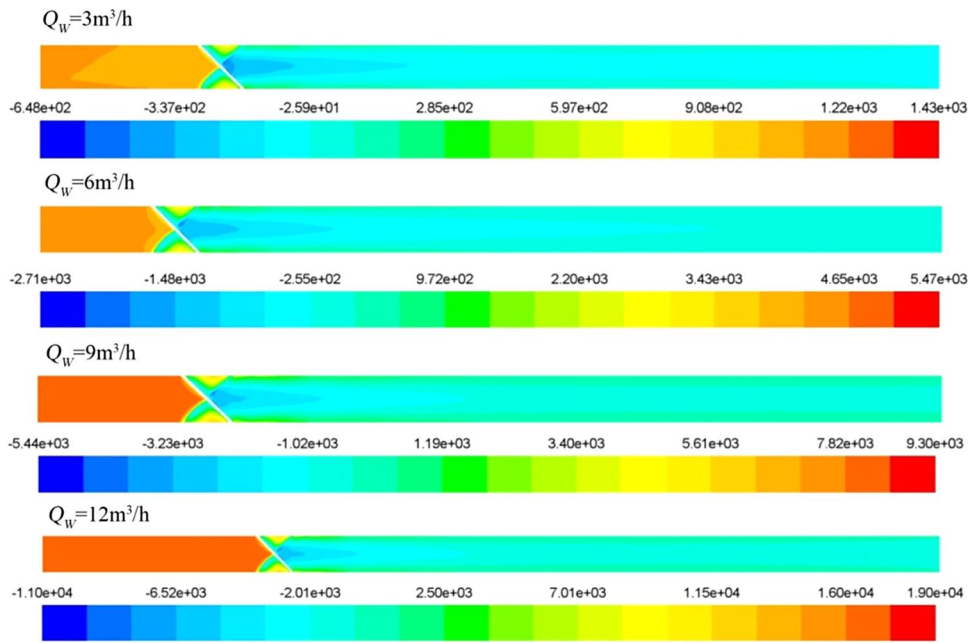

Figure 6. Pressure distribution at the location of section I ($Q_w = 12$ m³/h, $\beta = 0.107$).

$Q_w=3m^3/h$

$Q_w=6m^3/h$

$Q_w=9m^3/h$

$Q_w=12m^3/h$

Figure 7. Longitudinal pressure distribution of different inlet flow rates under inlet oil phase concentration of $\beta = 10.7\%$.

For the convenience of analysis, the geometric parameters are dimensionless and are normalized to the pipe inner diameter R. The total profiles for all the curvatures are almost symmetric. Though gravity exerts an influence, it is negligible compared to the strong rotational flow. It is clear that for the sections near the vane zone, the velocity at the pipe center is low. As the horizontal axis moves from the pipe center to the wall, the axial velocity gradually increases to the maximum value near the wall and then decreases to 0 abruptly. We note that for the section $4R$ after the vane zone, the velocity at the pipe center is

negative, implying the existence of a backflow. For the other sections, the velocities at the pipe center are positive and gradually increase, while the local maximal values gradually decrease. However, section $42R$ from the vane zone where axial values vary little except for the abrupt reduction at the wall is an exception to this trend. This means that the swirling zone is rather weak at the cross section $42R$ from the vane zone.

Figure 10 provides a detailed representation of the radial distribution of the tangential velocity. The total profiles are antisymmetric with the value of 0 at the pipe center. As the position moves from
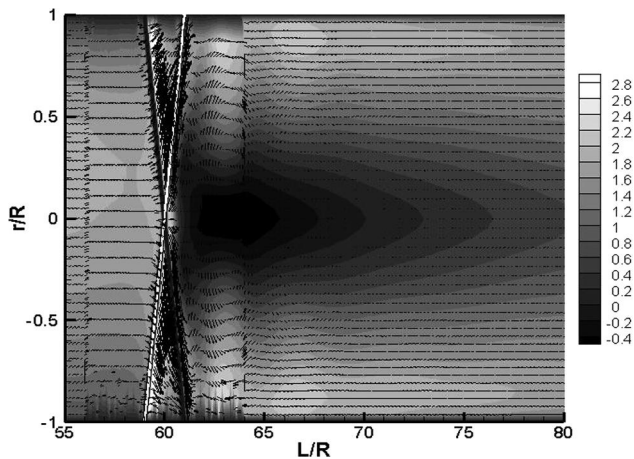
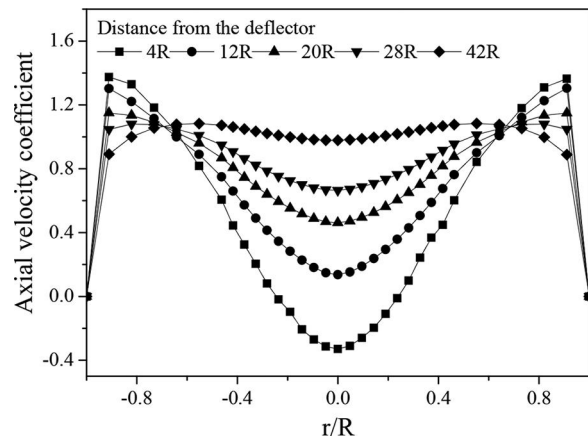**Figure 8.** Velocity in the longitudinal section ($Q_w = 9m^3/h$, $\beta = 0.107$).

Figure 9. Axial velocity coefficient in the cross section at different distances to the guide vanes ($Q_w = 9m^3/h$, $\beta = 0.107$).
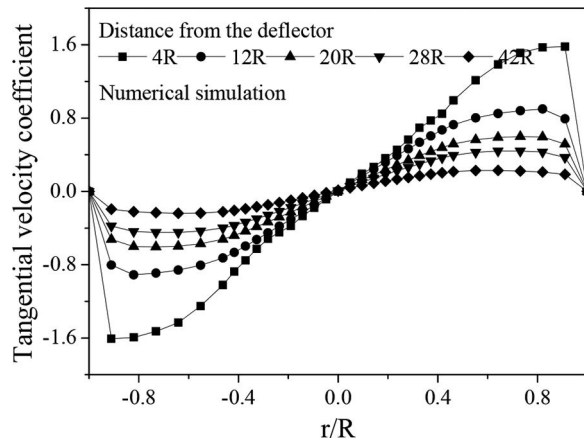
Figure 10. Tangential velocity coefficient in the cross section at different distances to the guide vanes for numerical simulation ($Q_w = 9m^3/h$, $\beta = 0.107$).

the pipe center to the inner wall, tangential velocity gradually increases to a maximum value near the inner wall with an abrupt decrease to 0 at the inner wall. Moreover, the maximum of the tangential velocity decreases when the sampling section moves away from the vane zone, which means that the intensity of the swirling flow attenuates axially.

As is done for the pressure distribution study, streamline distributions are also evaluated for all inlet flow rates as shown in Figure 11. In the stream line figures, the color map for different inlet flow rates is unified to a single color. A red color streamline indicates a higher velocity magnitude,

while the blue color indicates a lower velocity. The overall trends for the streamline of the various inlet flow rate operating conditions are almost the same. Uniformly distributed straight streamlines are guided and accelerated when flowing through the vane zone. Rotational streamlines characterizing the swirling flow field are obtained as the result. Similar to the curvatures for the streamline, velocity magnitudes gradually decrease as the fluids flow away from the vane zone. Comparison of the streamline figures of different inlet flow rates shows that the only difference is found in the maximal velocity magnitudes, which increase with the inlet flow rates.

To further analyze the characteristics of the swirling flow field, the swirl number (S) was obtained by the following equation (Ahmed et al., 2015):

$$S = \frac{W_b}{U_b} \quad (10)$$

where U_b and W_b are the bulk axial and tangential velocities, respectively, and are given by:

$$U_b = \frac{2}{R^2} \int_0^R r\langle u\rangle \mathrm{d}r \quad (11)$$

$$W_b = \frac{2}{R^2} \int_0^R r\langle w\rangle \mathrm{d}r \quad (12)$$

In this work, the swirl numbers obtained at sections 4R, 12R, 20R, 28R, and 42R downstream of the guide vanes were 1.31, 0.76, 0.55, 0.41, and
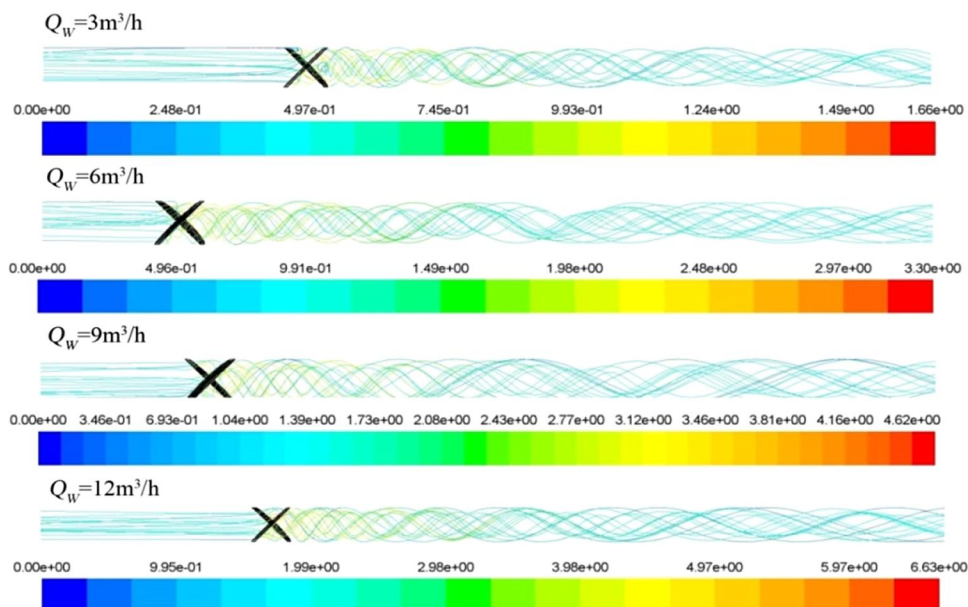

Figure 11. Streamline of different inlet flow rates under inlet oil volume concentration of $\beta = 10.7\%$.

0.28, respectively. That is, the swirl number decreases gradually with an increase in the distance to the guide vanes. This corresponds to the law of decreasing tangential velocity coefficient shown in Figure 10. Through the study described above, the hydrodynamic character of the fluid domain under operating conditions studied is elucidated, which is beneficial for further investigations and for the applications of this approach in industrial production.

Oil distribution

Another important factor affecting the separation efficiency is the oil distribution in the swirling flow field. In this section, the specific oil distribution is described by a combination of experimental measurements and numerical simulations.

Experimental measurements

Figure 12 depicts the oil distribution measured by ERT in the pipe cross section at the location of section II when the inlet water flow rate is 6 m^3/h and the inlet oil volume fraction is $\beta = 5.7\%$. The X and Y axes represent the proportions of the local radius to the pipe radius in the horizontal and vertical directions, respectively. The Z-axis represents the oil volume fraction at a particular position. In the figure, the red color represents a high local oil volume fraction, while the blue color represents a low local volume fraction with the other colors representing intermediate values. Obviously, the oil volume fraction at the center is much higher
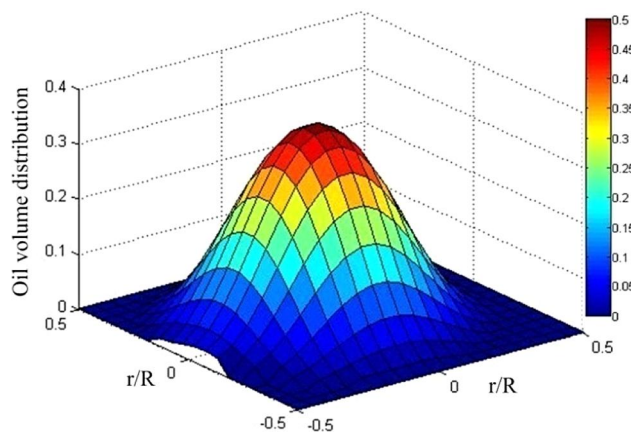

Figure 12. Oil volume distribution at the location of section II with 6 m^3/h water inlet flow rate and $\beta = 5.7\%$ inlet oil volume fraction.

than that near the pipe boundary. The peak oil volume fraction at the pipe center is almost 50%, while it remains 0 near the pipe wall. It can be seen that the oil core existed at the pipe center in the form of oil droplets mixed with water at the center. In addition, at the location away from the pipe center, almost pure water exists. Furthermore, similar phenomena are found under other working conditions. The oil core remains at a reasonable distance downstream of the vane zone.

Figure 13 shows the oil distribution at the location of section II with the water flow rate of $Q_w = 3$ m^3/h. The inlet oil volume fractions are 0, 0.057, 0.107, and 0.153, respectively. In Figure 13, the red center area is oil dominated, and the surrounding area with blue color is water dominated. In addition, the red oil core is an approximate circle. When the inlet oil volume fraction is zero, the cross section is full of water. As the inlet oil volume fraction increases, the oil core increases gradually. When the inlet oil volume fraction increases, the oil core becomes larger under the same centrifugal force.

Figure 14 shows the measured oil volume fraction distributions in the vertical direction at sections I and II. Here, the corresponding water flow rate is 3.0 m^3/h. It can be seen that the oil volume fraction curve increases with increasing inlet oil volume fraction. However, under the same conditions, the oil volume fraction in section II is much lower than that in section I, mainly because the vortex intensity is gradually weakened as the axial distance to the guide vanes increases. This phenomenon can be understood in different ways. According to the previous introduction, the axial velocity increases gradually with the increasing distance from the guide vanes. Therefore, to maintain the mass conservation of the oil phase, the oil volume fraction should decrease gradually. Moreover, at section I, the maximal oil volume fraction is located at approximately $r/R = 0$; however, at section II, the maximal oil volume fraction is located at $r/R < 0$. In other words, at section II, the oil core moves slightly above the pipe axis due to the combined effects of the centrifugal force and buoyancy. At section I, the centrifugal force is strong, and therefore the effects of buoyancy are not obvious. With increasing distance from the guide vanes, the centrifugal force decreases, and the oil core moves up gradually. Combined with the front
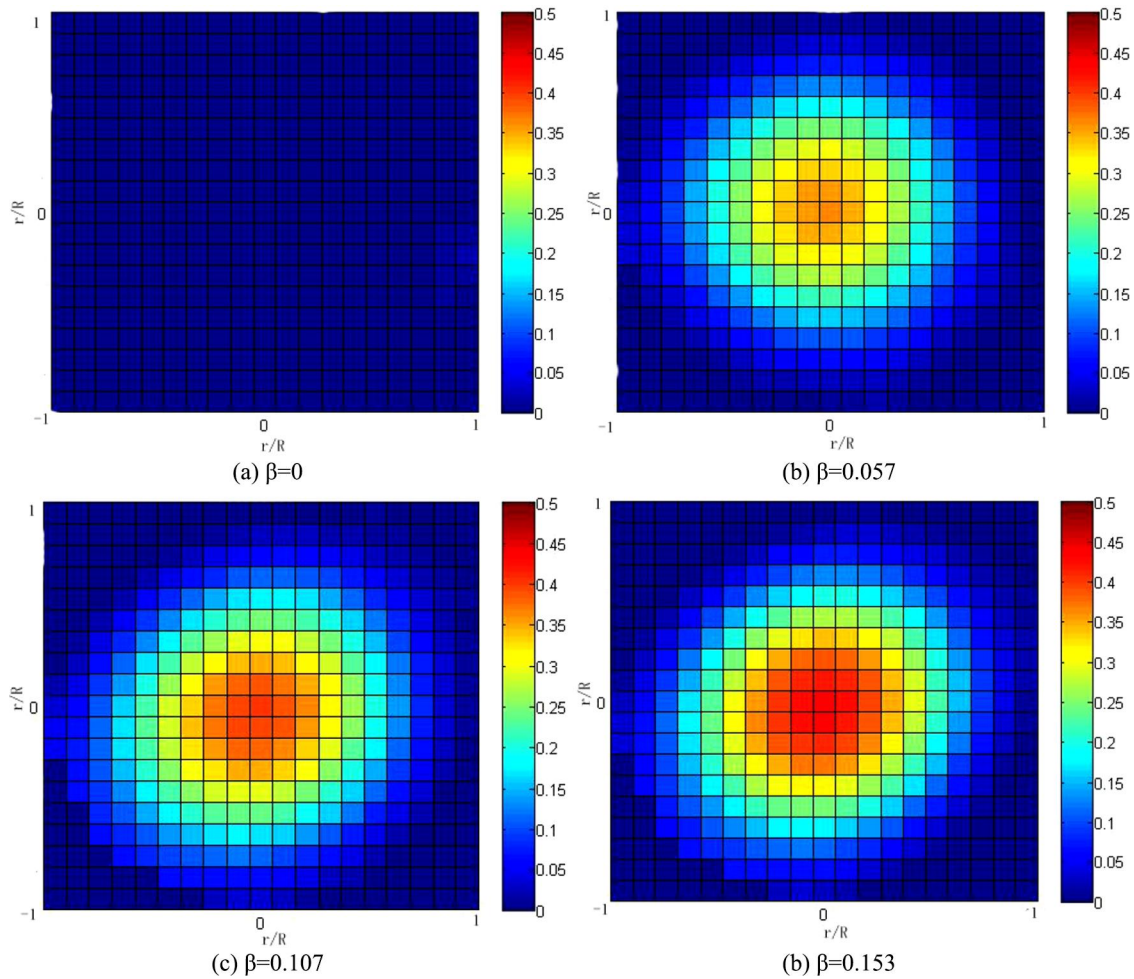
Figure 13. Oil volume distribution at the location of section II under different inlet oil volume fractions.

study of the flow velocities, the conclusion can be made that buoyancy influences the oil distribution but has little influence on the velocity distribution.

Figure 15 depicts the oil distribution in the vertical direction with the constant inlet oil volume fraction of $\beta = 0.107$. The inlet water flow rate shows a major impact on the oil distribution at section I. As the water flow rate increases, the oil volume fraction curve becomes lower and more gradual because the oil is more likely to form an
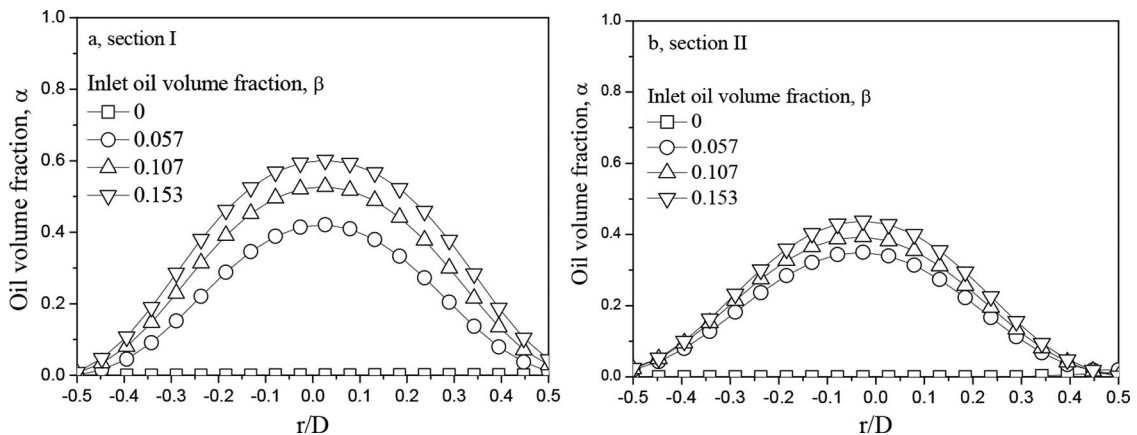

Figure 14. Oil volume distribution in the vertical direction with water flow rate of $Q_w = 3\,m^3/h$.
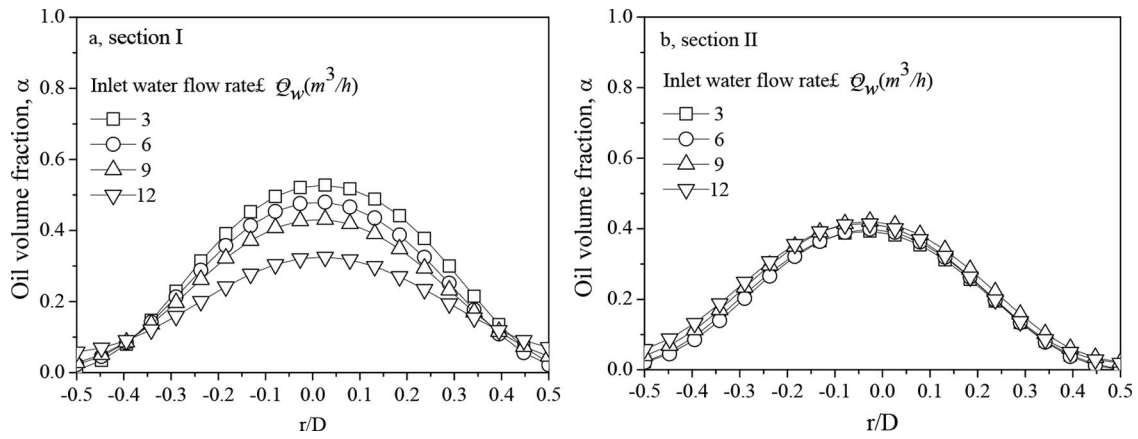
Figure 15. Oil volume distribution in the vertical direction with the inlet oil content of $\beta = 0.107$.

emulsion with a large water flow rate. Once the emulsion is formed, the efficiency of the centrifugal separation is greatly reduced. For section II, however, the change of the water flow rate had no significant effect. The average oil volume fraction in the pipe cross section was obtained by integrating the measured oil volume fractions of each pixel.

Numerical simulations

Figure 16 shows the specific oil distribution at section I obtained by the CFD simulation. Here, the water flow rate is $Q_w = 9$ m³/h and the inlet oil volume fraction is $\beta = 0.107$. The oil volume fraction is clearly higher at the pipe center. For the corresponding oil distribution in the longitudinal section, the domain covers the area from 5R

upstream to 20R downstream of the guide vanes. Downstream of the guide vanes, the maximal oil volume fraction is located at the center of the pipe. From the pipe center to the pipe inner wall, the oil volume fraction gradually decreases. Near the pipe inner wall, the oil volume fraction is approximately zero, which means that oil is entirely absent. That is, in the swirling flow field induced by the guide vanes, oil is more likely to move to the center area of the pipe.

The influence of the distance on the oil distribution is presented in Figure 17. Here, the water flow rate is $Q_w = 9$ m³/h and the inlet oil volume fraction is $\beta = 0.107$. The distances between the cross section and the guide vanes are 4R, 12R, 20R, 28R, and 42R. All oil distributions within the cross sections are similar. As the distance to
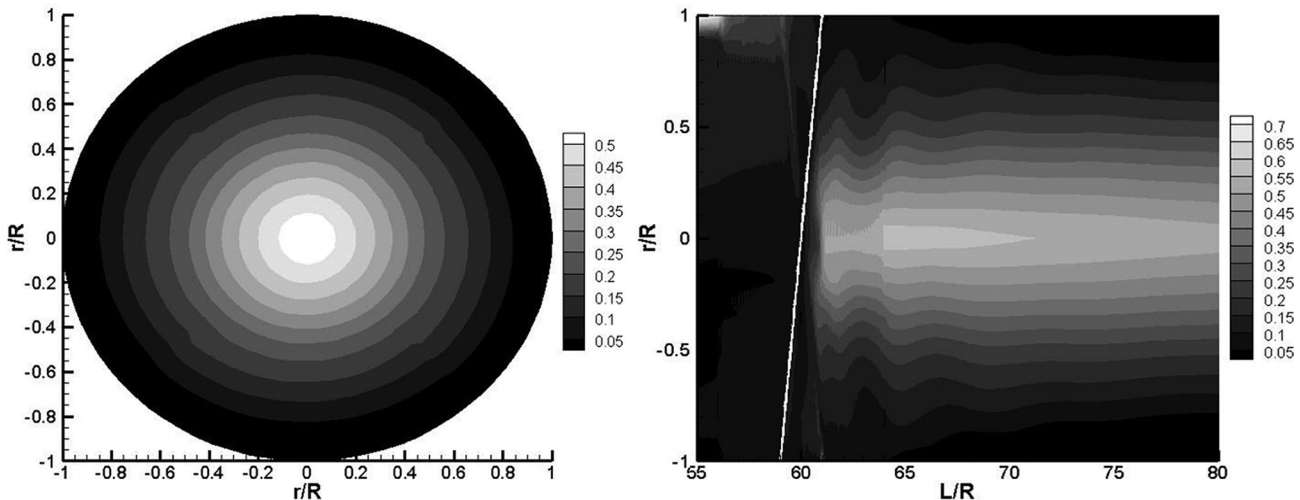

Figure 16. Oil volume distribution in the cross section at section I and in the longitudinal section ($Q_w = 9$ m³/h, $\beta = 0.107$).
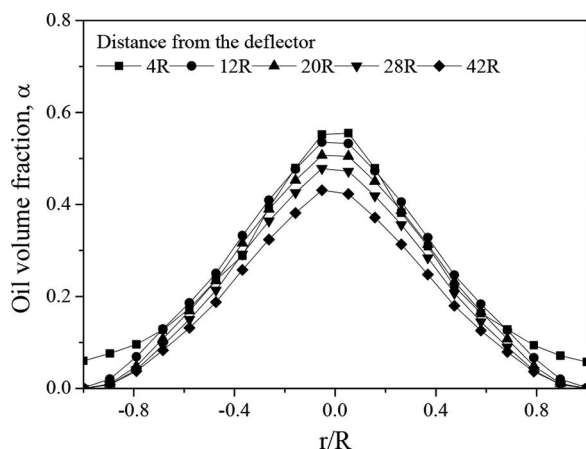
Figure 17. Oil volume distribution in the cross section at different distances to the guide vanes ($Q_w = 9m^3/h$, $\beta = 0.107$).

the guide vanes increases, the oil volume fraction gradually decreases because the swirling intensity gradually becomes weaker due to viscous dissipation. However, the decrease in the oil volume fraction is modest, which means that the oil core is maintained for a period of time, potentially allowing for efficient oil–water mixture separation.

Conclusion

Vane-type pipe separators can realize the centrifugal separation of oil and water using guide vanes to produce swirling flow fields. In the present study, the flow characteristics of the swirling flow field induced by the guide vanes were studied experimentally and numerically, and the following concluding points were obtained:

The two phases of the water and oil mixture move in the same axial direction for this type of flow field, which is very different from the behavior of a traditional hydrocyclone with a tangential inlet. The smallest axial velocity and tangential velocity are located at the center of the pipe behind the guide vanes. From the center to the wall, both the pressure and velocities increase gradually. Downstream of the guide vanes, the maximal oil volume fraction is located at the center of the pipe. From the pipe center to the pipe inner wall, the oil volume fraction gradually decreases. As the distance to the guide vanes increases, the oil volume fraction gradually decreases. This study proves the possibility of efficient oil–water mixture

separation by the guide vanes, and the results may be of great significance for guiding the optimal design of vane-type pipe separators.

ORCID

Jing-yu Xu ⓘ http://orcid.org/0000-0002-1058-2257

References

Ahmed, Z. U., Al-Abdeli, Y. M., and Guzzomi, F. G. (2015). Impingement pressure characteristics of swirling and non-swirling turbulent jets, *Exp. Therm. Fluid Sci.*, **68**, 722–732.

Gao, S. L., Wei, D. Z., Liu, W. G., Ma, L., Lu, T., and Zhang, R. (2011). CFD numerical simulation of flow velocity characteristics of hydrocyclone, *Trans. Nonferrous Met. Soc. China*, **21**(12), 2783–2789.

Javadi, A., Bosioc, A., Nilsson, H., Muntean, S., and Susan-Resiga, R. (2016). Experimental and numerical investigation of the precessing helical vortex in a conical diffuser, with rotor-stator interaction, *J. Fluids Eng.*, **138**(8), 081106.

Li, H., Wang, M., Wu, Y. X., Ma, Y., and Williams, R. A. (2005). Measurement of oil volume fraction and velocity distributions in vertical oil-in-water flows using ERT and a local probe, *J. Zhejiang Univ., Sci., A*, **6**(12), 1412–1415.

Marins, L. P., Duarte, D. G., Loureiro, J. B., Moraes, C. A. C., and Silva Freire, A. P. (2010). LDA and PIV characterization of the flow in a hydrocyclone without an air-core, *J. Pet. Sci. Eng.*, **70**(3–4), 168–176.

Maxwell, J. C. (1881). *A Treatise on Electricity and Magnetism*, Clarendon Press, Oxford, UK.

Olerni, C., Jia, J., and Wang, M. (2013). Measurement of air distribution and void fraction of an upward air-water flow using electrical resistance tomography and wire-mesh sensor, *Meas. Sci. Technol.*, **24**(3), 35403–35411.

Shi, S. Y., and Xu, J. Y. (2015). Flow field of continuous phase in a vane-type pipe oil-water separator, *Exp. Therm. Fluid Sci.*, **60**, 208–212.

Shi, S. Y., Xu, J. Y., Sun, H. Q., Zhang, J., Li, D. H., and Wu, Y. X. (2012). Experimental study of a vane-type pipe separator for oil-water separation, *Chem. Eng. Res. Des.*, **90**(10), 1652–1659.

Wang, M., Jones, T. F., and Williams, R. A. (2003). Visualization of asymmetric solids distribution in horizontal

swirling flows using electrical resistance tomography, *Chem. Eng. Res. Des.*, **81**(8), 854–861.

Wang, Z. B., Ma, Y., and Jin, Y. H. (2011). Simulation and experiment of flow field in axial-flow hydrocyclone, *Chem. Eng. Res. Des.*, **89**(6), 603–610.

Wang, M., Mann, R., and Dickin, F. (1999). Electrical resistance tomographic sensing systems for industrial applications, *Chem. Eng. Commun.*, **175**, 49–70.

Wannassi, M., and Monnoyer, F. (2016). Numerical simulation of the flow through the blades of a swirl generator, *Appl. Math. Model.*, **40**(2), 1247–1259.

Wu, Y-x., Li, H., Wang, M., and Williams, R. A. (2005). Characterization of air-water two-phase vertical flow by using electrical resistance imaging, *Can. J. Chem. Eng.*, **83**, 37–41.

Zhou, N., Gao, Y., An, W, and Yang, M. (2010). Investigation of velocity field and oil distribution in an oil-water hydrocyclone using a particle dynamics analyzer, *Chem. Eng. J.*, **157**(3), 73–79.